



MnO/reduced graphene oxide sheet hybrid as an anode for Li-ion batteries with enhanced lithium storage performance

Y.J. Mai, D. Zhang, Y.Q. Qiao, C.D. Gu, X.L. Wang, J.P. Tu*

State Key Laboratory of Silicon Materials and Department of Materials Science and Engineering, Zhejiang University, Hangzhou 310027, China

HIGHLIGHTS

- MnO/RGOS hybrid is synthesized by a two-step electrode design.
- As an anode material, it displays superior lithium storage performance.
- Reasons for such enhanced performance are investigated by TEM, GITT and EIS.
- The probable origins of hysteresis in voltage are discussed.

ARTICLE INFO

Article history:

Received 13 November 2011

Received in revised form

8 May 2012

Accepted 28 May 2012

Available online 1 June 2012

Keywords:

Manganese monoxide

Graphene

Hybrid

Lithium ion battery

ABSTRACT

Relatively small hysteresis in voltage, appropriate electromotive force and low average delithiation voltage make MnO, among many transition metal oxides. MnO/reduced graphene oxide sheet (MnO/RGOS) hybrid is synthesized by a two-step electrode design consisting of liquid phase deposition of MnCO₃ nanoparticles on the surface of graphene oxide sheets followed by heat treatment in flowing nitrogen. As an anode for Li-ion batteries, the MnO/RGOS hybrid electrode shows a reversible capacity of 665.5 mA h g⁻¹ after 50 cycles at a current density of 100 mA g⁻¹ and delivers 454.2 mA h g⁻¹ at a rate of 400 mA g⁻¹, which is obviously better than that of bare MnO electrode. Those reasons for such enhanced electrochemical properties are investigated by galvanostatic intermittent titration technique (GITT) as well as electrochemical impedance spectroscopy (EIS). The probable origins, in the term of thermodynamic and kinetic factors, for the marked hysteresis in voltage observed between charge and discharge are also discussed.

© 2012 Elsevier B.V. All rights reserved.

1. Introduction

The use of several transition metal oxides (TMO) that react with lithium through heterogeneous conversion reactions holds the promise of higher energy density Li-ion batteries (LIBs) [1,2]. However, conversion-type electrodes still suffer from a marked hysteresis in voltage between charge and discharge, resulting in poor energy efficiency and voltages. Recently, we reported the synthesis of NiO-reduced graphene oxide sheet (RGOS) hybrid for LIBs in which the lithium storage performance of NiO was enhanced with the corporation of RGOS [3]. However, the introduction of RGOS, like many other conducting additives such as carbon coating, carbon nanotubes and acetylene black, is not very effective to decrease the hysteresis in voltage which is as large as 1.0 V [3].

Before obtaining some effective measures to tackle such systematic hysteresis, it is necessary to find the appropriate oxides among the TMO with small hysteresis to increase the round-trip efficiency of the conversion-type electrodes. MnO is considered as a possible alternative due to its relatively smaller hysteresis in voltage (0.7 V) observed between charge and discharge. Such hysteresis of course is much larger than that of insertion-type (e.g. graphitic carbon and Li₄Ti₅O₁₂, less than 0.2 V) and alloying-type (silicon, 0.3 V; nano-SnSb, 0.5 V) of electrode systems [4]. However, most TMO conversion-type electrodes still suffer from a large hysteresis of more than 1 V [5]. There are two other advantages for MnO as an anode material for LIBs. Firstly, the average delithiation voltage is about 1.2 V [6,7], which is favorable for increasing the energy density. This value is higher than that of graphite (0.3 V), silicon (0.6 V), Sn (0.7 V) [4,8], but still lower than that of CoO (1.8 V) [1], FeO (1.6 V) [1], NiO (1.9 V) [9], CuO (2.1 V) [10], Co₃O₄ (2.0 V) [11] and Li₄Ti₅O₁₂ (1.6 V) [12]. Secondly, it possesses an appropriate electromotive force (emf) of 1.032 V, which is favorable for

* Corresponding author: Tel.: +86 571 87952856; fax: +86 571 87952573.

E-mail addresses: tujp@zju.edu.cn, tujplab@zju.edu.cn (J.P. Tu).

complete lithium uptake because most TMO show an overpotential around 1 V for the lithium uptake reaction at the plateau region [5].

Unfortunately, like many other TMO, MnO still suffers from small reversible capacity and poor cyclic stability. Two main reasons include the poor transport property for electrons within the active material and the loss of electronic contact between active particles as a consequence of large volume expansion/contraction associated with the lithium uptake/extraction process. A variety of appealing strategies have been used to solve these intractable problems, such as decreasing particle size [7], MnO/C core-shell nanorods [13], coaxial MnO/C nanotubes [14] and MnO/C nanocomposites [15,16].

Recently, lithium metal alloys [17–19] or metal oxide nanoparticles [20–23] have been hybridized with RGOS for LIBs due to its superior electronic conductivity, structural flexibility, large surface area and chemical stability. Such RGOS-based nanostructure electrodes display higher specific capacity and better cyclic stability compared to naked particle electrodes. In the above structures, on one hand, RGOS not only work as templates for anchoring well-dispersed nanoparticles and act as a highly conductive matrix for realizing efficient conduction of charge carriers but also can effectively accommodate the volumetric changes and considerably reduce the aggregation of nanoparticles during lithium insertion/extraction process. On the other hand, the nanoparticles in turn prevent the re-stacking and, to some extent, expand the space of the graphene layers, keeping their high active surface area and increasing the lithium storage performance of RGOS electrodes. Therefore, it is believed that the hybrid electrode of flexible and electrically conductive RGOS anchored with MnO nanoparticles can efficiently utilize the combinative merits of nanosized MnO and RGOS and thus exhibits superior lithium storage performance.

In this present work, firstly, the MnO/reduced graphene oxide sheet hybrid (referenced as MnO/RGOS) is synthesized by a two-step electrode design consisting of liquid phase deposition of MnCO₃ nanoparticles on the surface of graphene oxide sheets followed by the heat treatment in flowing nitrogen. In addition, the lithium storage performances of the as-prepared hybrid, as an anode material for LIBs, are investigated and those reasons for such enhanced electrochemical properties are also studied. Finally, the probable origins, in the term of thermodynamic and kinetic factors, for the marked hysteresis in voltage observed between charge and discharge are also discussed.

2. Experimental

MnO/RGOS hybrid was prepared as follows. First of all, 140 mg graphene oxide sheets were dispersed in 140 ml deionized water by sonication for 30 min. The graphene oxide sheets were obtained by a modification of Hummers' method with graphite flakes as the starting material [24]. Ethanol (25 ml) was then added into the above graphene oxide sheet suspension with stirring until complete dispersion. MnSO₄ solution (0.03 M, 115 ml) and NH₄HCO₃ solution (0.3 M, 115 ml) were slowly and simultaneously added into the above suspension and then stirred for 4 h at room temperature. The obtained precursor was separated by centrifugation and washed several times with deionized water. Then it was collected by freezing drying and finally calcined in a tube furnace at 600 °C for 1 h in flowing nitrogen to obtain the MnO/RGOS hybrid.

The as-prepared hybrid was characterized by means of X-ray diffraction (XRD, D/max 2550-PC), transmission electron microscopy (TEM, Tecnai F20 and JEM 2100F). Thermogravimetry (TG, SDT Q600 V8.2 Build 100) analysis from room temperature to 700 °C at a heating rate of 10 °C min⁻¹ in air was carried out to estimate the content of RGOS in the hybrid material. Raman spectroscopy was

recorded over the frequency range of 200–2000 cm⁻¹ using a Jobin-Yvon Labor Raman HR-800 system (514.5 nm). The beam intensity is 10 mW and the duration is 30 s.

The working electrodes were prepared by a slurry coating procedure. The slurry consisting of 80 wt.% active materials (MnO/RGOS or commercial MnO, Alfa, 99%), 10 wt.% acetylene black and 10 wt.% polyvinylidene fluorides dissolved in *N*-methyl pyrrolidinone was incorporated on nickel foam with 15 mm in diameter. The electrolyte was 1 M LiPF₆ in ethylene carbonate–dimethyl carbonate (1: 1 in volume). CR-2025-type coin cells were assembled in a glove box under argon atmosphere. The galvanostatic discharge/charge measurements were conducted on LAND battery program-control test system between 0.02 and 3.0 V at room temperature (25 ± 1 °C). Given the fact that lithium also can be reversibly stored in RGOS, the specific charge/discharge current density and the specific capacity are based on the whole weight of MnO and RGOS. Cyclic voltammetry (CV) measurements were performed on a CHI660C electrochemical workstation with a scan rate of 0.1 mV s⁻¹ between 0 and 3 V (versus Li/Li⁺). Galvanostatic intermittent titration technique (GITT) experiments were also performed on LAND battery program-control test system by charging/discharging the cells for 2 h at a rate of C/20 of the theoretical capacity of MnO (755 mA h g⁻¹). The relaxation period was set as 4 h. Electrochemical impedance spectroscopy (EIS) measurement was carried out in the frequency range from 0.01 Hz to 100 kHz on a CHI660C electrochemical workstation.

3. Results and discussion

Fig. 1a shows the XRD patterns of the as-prepared hybrid and the commercial MnO powders. For the former, with the exception of the reflections owing to RGOS, all Bragg peaks are consistent with those of MnO phase (JCPDS 07-0230). It is found that the choose of MnCO₃, instead of Mn(OH)₂, as the precursor of MnO is important to obtain pure MnO phase because Mn(OH)₂ is easy to be oxidized to MnO(OH)₂ in the air during the process of liquid phase deposition. It is noticed that the (002) characteristic diffraction peak of RGOS, appearing at 2θ of around 25° is very weak and broad, suggesting disordered stacking and less agglomeration for RGOS in the hybrid material. Similar phenomenon was also observed in other RGOS hybrid materials [18,20,22,25,26].

Fig. 1b shows the Raman spectrum of the MnO/RGOS hybrid. MnO easily transforms into Mn₃O₄ because of a local heating effect and photochemically induced transformations under beam irradiation when the beam intensity is more than 1.1 mW during the Raman measurement [27]. Thus, the strong vibrational band at 648 cm⁻¹ and bands below 400 cm⁻¹ belong to Mn₃O₄ rather than MnO. Before thermal reduction (the inset of Fig. 1b), similar to what have been reported for graphene oxide sheets [24,28] and graphene oxide nanoribbons [29,30], the G-band at 1594 cm⁻¹ broadens with the appearance of the D band at 1356 cm⁻¹. Also the position of the G-band shifts to higher frequencies compared to that of highly oriented pyrolytic graphite (1582 cm⁻¹). This indicates that the layer number of graphene oxide sheets is obviously decreased given that the position of the G-band upshifts with the decreasing of graphene layer number [31,32]. After thermal reduction, the ratio of the intensity of D peak to G peak increases, which is in agreement with previous reports [28,29,33]. It is hypothesized that thermal reduction decreases the spatial dimensions of the sp² regions of RGOS, but increases their overall presence in the material, resulting in an enhancement of electrical conductivity.

As shown in Fig. 1c, the product of MnO/RGOS after calcining at 700 °C in air is Mn₂O₃. Therefore, it is reasonable to believe that the gradual weight increase in the thermogravimetry analysis curve (Fig. 1d), starting from 300 up to 350 °C corresponds to the

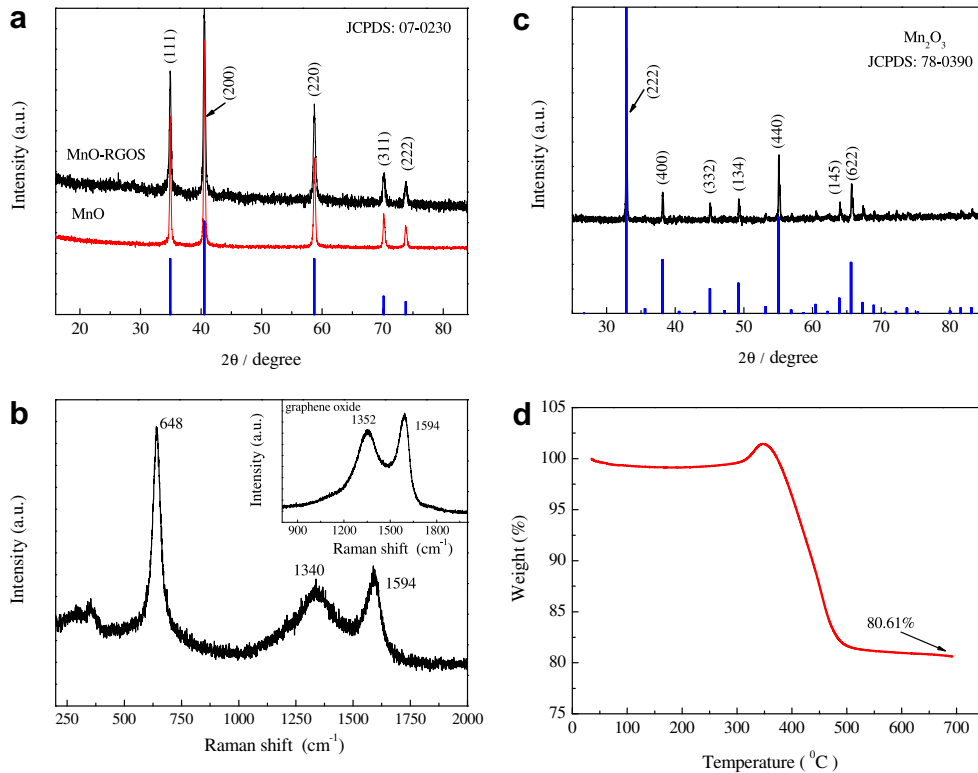


Fig. 1. (a) XRD patterns of MnO and MnO/RGOS powders. (b) Raman spectrum of MnO/RGOS, and the inset is the Raman spectrum of graphene oxide, (c) XRD patterns of the product of MnO/RGOS after calcining at 700 °C in air for 3 min and the heating rate is 10 °C min⁻¹ and (d) TGA curve of MnO/RGOS hybrid.

synthetical effect between the oxidation of MnO into Mn₂O₃ and the partial loss of RGOS. When the temperature is higher than 500 °C, the RGOS are completely combusted. Therefore, the weight percentage of RGOS in the as-prepared hybrid is about 72.5%.

Fig. 2 shows TEM images of the MnO/RGOS hybrid. The smooth surfaces of the pristine graphene oxide sheets (the inset of Fig. 2a) are homogeneously covered by many nanoparticles (Fig. 2a). The RGOS are comprised of 35 layers, and the nanoparticles obtained are up to several nanometers in size (Fig. 2b). As shown in the inset of Fig. 2b, some of them show clear lattice fringes and the stripe distance is about 0.256 nm, closed to *d*-value of (111) plane of MnO. In order to better understand the effect of the microstructure of MnO/RGOS hybrid on its electrochemical performance, the MnO/RGOS hybrid cycled 50 times at a current density of 100 mA g⁻¹ is also investigated by TEM. For comparison, the cycled MnO electrode is also presented. After 50 cycles, some cracks are observed in the MnO particles (Fig. 2c), which should be the result of large volumetric changes associated with the lithium uptake/extraction. Higher resolution observation reveals the disintegration of the initial particles with the formation of many smaller particles which are separated by some amorphous regions as shown by white arrows in Fig. 2d. Therefore, it is conceivable that electronic contact between the active materials could be a problem for the MnO electrode. Indeed, the stripe distance of some tiny grains is about 0.225 nm which can be assigned to (220) plane of β -Mn (33-0887) with a *d*-value of 0.223 nm, indicating that only part of Mn are reoxidized to MnO during the charge process. This observation can explain potential versus capacity traces presented in Figs. 4a and 5a with the capacity loss recorded between the first discharge and charge. For the MnO/RGOS hybrid, MnO nanoparticles are still homogeneously anchored on the surface of RGOS after 50 cycles. This indicates the elastic and flexible RGOS can accommodate the

volumetric changes of MnO nanoparticles upon Li uptake/extraction, maintaining the structure integrity of the as-prepared hybrid.

Just like many TMO, MnO reacts with lithium through a heterogenous conversion reaction, which is well demonstrated by Li and co-workers [6,7,34]. As shown in Fig. 3, both the CV curves of MnO and MnO/RGOS electrodes reflect the reaction mechanism. In the first cycle, a main cathodic peak and a weak cathodic peak are observed at 0.013 V and 0.5 V for the MnO/RGOS electrode and at 0.003 V and 0.5 V for the MnO electrode, corresponding to the conversion of MnO into a Mn/Li₂O nanocomposite and the formation of SEI films. The anodic peak at 1.32 V for MnO/RGOS and at 1.33 V for MnO is ascribed to the regeneration of MnO nanograins. In the second cycle, the main reduction peak is shifted to 0.42 V for MnO/RGOS hybrid and to 0.43 V for MnO. However, the positions of oxidation peaks for both the electrodes are almost unchanged. They are 1.33 V for MnO/RGOS and 1.35 V for MnO, respectively. It is noticed that both the peak intensity and the integral areas of the MnO/RGOS electrode are larger than those of MnO electrode, indicating that the incorporation of RGOS enhances the reaction kinetics and active materials utilization.

Fig. 4a and b presents the potential versus capacity traces of MnO and MnO/RGOS electrodes at the current density of 100 mA g⁻¹, respectively. In the first discharge, a well-defined conversion plateau at 0.1 V (vs. Li⁺/Li) is observed for the MnO electrode. Such plateau, however, is replaced by a sloping curve at a potential range of 0.1–0.25 V (vs. Li⁺/Li) for the MnO/RGOS electrode, which is slightly closer to the emf, indicating a smaller polarization for the latter. For both electrodes, the second discharge profiles are closer to that of the first charge than to the first discharge indicating the polarization of the second cycle is obviously smaller than that of the first cycle. In fact, this phenomenon is observed in many TMO electrodes that electrochemically react with

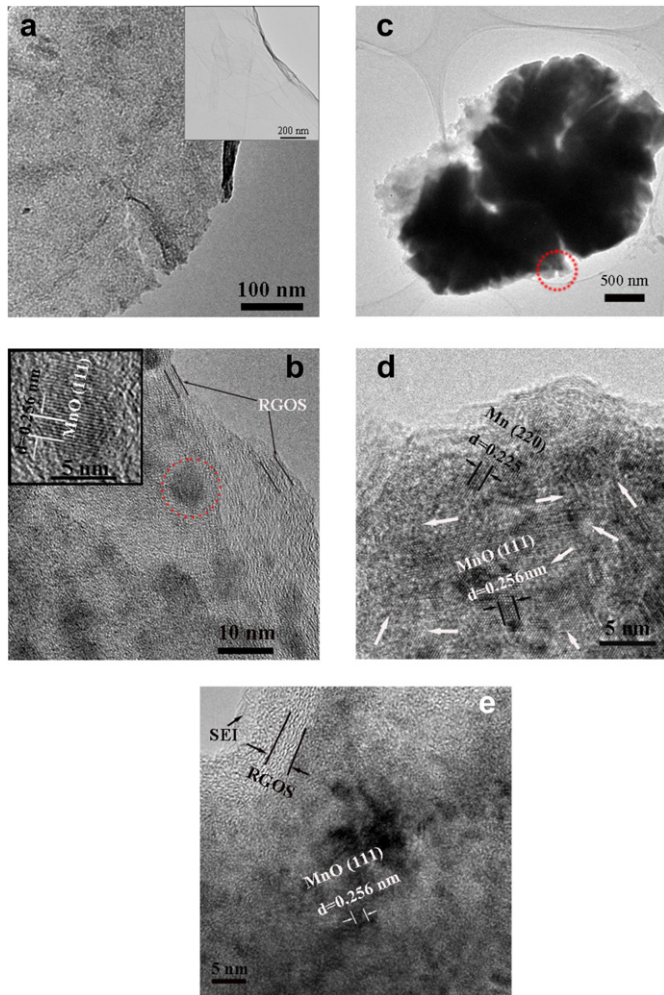


Fig. 2. (a) Low and (b) high magnification TEM images of MnO/RGOS hybrid, the inset of (a) is TEM image of graphene oxide and the inset of (b) is HRTEM of an individual particle anchored on the surface of RGOS, which is indicated by a red circle in Fig. 2b. (c) Low magnification TEM image of cycled MnO particle (charged to 3.0 V) and (d) the corresponding HRTEM image of the small area indicated by a red circle in Fig. 2c, in which the white arrows indicate some amorphous regions. (e) HRTEM image of the cycled MnO/RGOS hybrid (For interpretation of the references to color in this figure legend, the reader is referred to the web version of this article.).

lithium through conversion reactions which can be ascribed to larger surface area and smaller energy penalty of surface/interface energy because of the disintegration of the initial particles into nanoparticles after the initial conversion [5,35]. However, a significant hysteresis in voltage (0.7 V) remains and stays somewhat constant upon further cycling for both the electrodes, indicating that the introduction of RGOS is not very effective to decrease the hysteresis in voltage. Many previous studies suggested that enhancement of electronic wetting resulted in minor changes for the hysteresis in voltage, such as the carbon-coated MnO powder [7,14] and Fe₃O₄-based Cu nano-architected electrodes [36], and net-structured NiO–C nanocomposite [9]. It is found that the MnO/RGOS hybrid electrode exhibits an enhanced reversible capacity with respect to that of MnO electrode. For example, it respectively delivers an initial discharge capacity of 1001 mA h g⁻¹ and an initial charge capacity of 647.7 mA h g⁻¹. For the MnO electrode, however, they are decreased to 858.6 and 435.2 mA h g⁻¹, respectively. It is noteworthy that the RGOS are capable of storing lithium, and as what we previously reported, its lithium storage performance could be enhanced after the surface modification by Ni

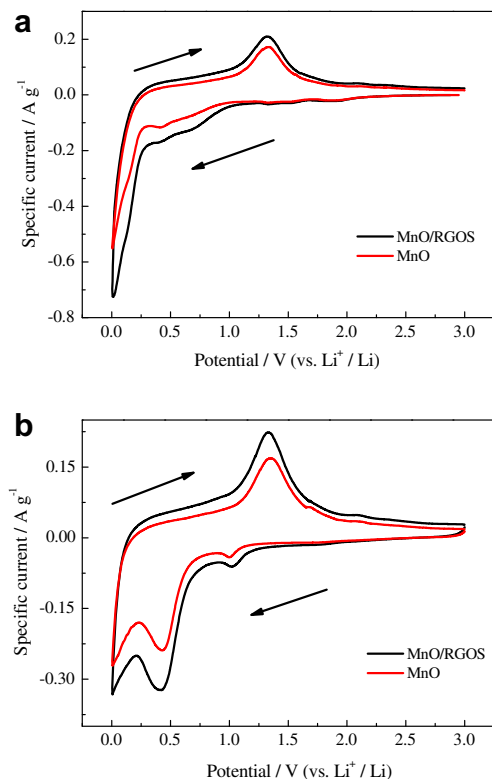


Fig. 3. CV curves of MnO and MnO/RGOS electrodes for (a) the first cycle and (b) the second cycle.

nanoparticles [37]. However, similar to the many graphene–metal oxide nanostructure electrodes for LIBs, there is a synergistic effect between MnO nanoparticles and RGOS in the hybrid electrode [20–23]. And there is no obvious trace which can be assigned to RGOS electrode that electrochemically reacts with lithium in the potential–capacity profiles for the MnO/RGOS hybrid electrode. Consequently, it is difficult to distinguish the electrochemical capacity contribution of RGOS from that of MnO in the total capacity of MnO/RGOS electrode and in this work the specific capacity of MnO/RGOS hybrid electrode is calculated based on the whole weight of MnO and RGOS. In addition, it can be imagined by analogy the NiO–graphene hybrid electrode that the content of graphene in hybrid electrode significantly affects the lithium storage performance of hybrid electrode [3]. If the content of RGOS is too high, the specific capacity of the hybrid electrode is decreased because the reversible specific capacity of RGOS is lower than the theoretical capacity of MnO. However, if the content of graphene is too low, its functions including buffer zone of volumetric changes as well as electron transfer medium, are decreased because there is not enough space to anchor the nanoparticles. Based on the present lithium storage performance of the MnO/RGOS electrode, it is reasonable to believe the present content of RGOS is a relatively optimized value. Of course, detained dates are needed and these works are on going.

Fig. 4c compares the cyclic performance of MnO and MnO/RGOS electrodes at a current density of 100 mA g⁻¹. For the MnO electrode, the reversible capacity continuously decays as the cyclic number goes by and after 20 cycles it levels off with a capacity of about 260 mA h g⁻¹, consistent with the previous reports [7,14]. It is believed that such capacity decay results from particle isolation and cracking, which are observed by TEM (Fig. 2c and d), as a consequent of entail massive structural reorganization and volumetric changes of MnO during the lithium uptake/extraction. In contrast,

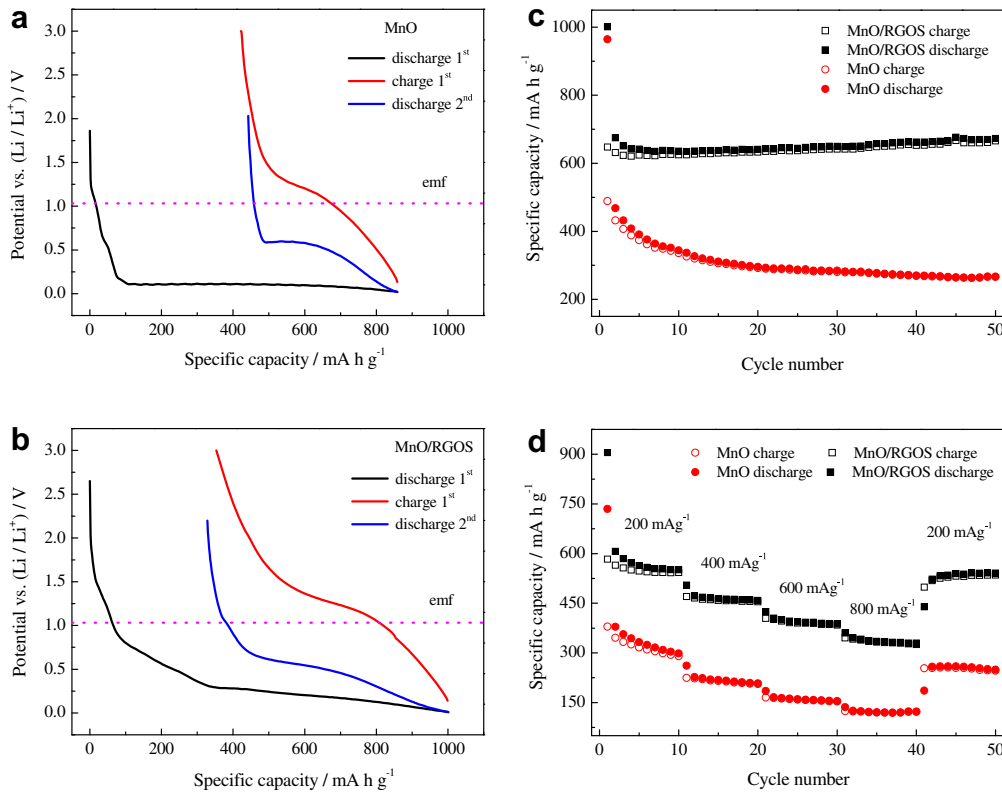


Fig. 4. Potential versus capacity traces of (a) MnO and (b) MnO/RGOS electrode, (c) cyclic performance at a current density of 100 mA g^{-1} and (d) rate performance.

for the MnO/RGOS electrode, well-crystallized MnO nanoparticles are still homogeneously anchored on the surface of RGOS after 50 cycles, as shown in Fig. 2e. Such good microstructure stability should benefit the cyclic stability. Indeed, the capacity remains constant or even slightly increases after 50 cycles for the MnO/RGOS electrode. It is noteworthy that the phenomenon that capacity slightly increases with the increasing of the cyclic number is also observed in carbon-coated MnO electrode [7], Co_3O_4 /RGOS electrode [22], nano-flaky MnO_2 /carbon nanotube nanocomposites [38] and $\text{CoO}-\text{Li}_2\text{O}$ [39] thin film electrodes. The origin is still not clear, and may be attributed to the formation of SEI layer or high oxidation state products.

Fig. 4d presents the rate capability of MnO and MnO/RGOS electrodes. In the case of hybrid electrode, the initial charge capacity is $583.4 \text{ mA h g}^{-1}$ and the reversible charge capacity is stable at $542.5 \text{ mA h g}^{-1}$ after 5 cycles at a current density of 200 mA g^{-1} , whereas the reversible capacity of MnO continuously decays from $379.6 \text{ mA h g}^{-1}$ to $290.1 \text{ mA h g}^{-1}$. Upon increasing the discharge/charge current density to 400 and 800 mA g^{-1} , the reversible capacity of MnO/RGOS electrode still maintains at 454.2 and $325.6 \text{ mA h g}^{-1}$, respectively. What's more, the MnO/RGOS electrode can regain higher capacity and better cyclic stability compared with the MnO electrode by reverting to the lower current rates of 200 mA g^{-1} after 40 cycles. Such performance is poorer than that of the carbon-coated porous MnO microspheres [34], but is better than that of carbon-coated milled MnO [7], MnO/C core-shell nanorods [13], coaxial MnO/C nanotubes [14] and MnO/C nanocomposites [15,16].

In order to understand the reasons of the improved electrochemical performance for MnO/RGOS electrode with respect to the MnO electrode, GITT measurements of both electrodes are carried on. As shown in Fig. 5a, two distinct regions are observed in

the first discharge profile for the MnO electrode. A long plateau appears at around 0.18 V , followed by a sloped region down to 0.02 V . The capacity contribution of the long plateau region can be assigned to the transformation of MnO to $\text{Mn}/\text{Li}_2\text{O}$ nanocomposite, and the sloped region can be assigned to the interfacial charging mechanism, which has been explained by Maier et al. [40–43]. In fact, the capacity contribution of sloped region is easier to be noticed after the first discharge. The Li storage capacities of the first discharge and charge are 936.9 and $468.5 \text{ mA h g}^{-1}$, corresponding to an initial coulombic efficiency of 50.1% . On the other hand, the MnO/RGOS electrode delivers a discharge capacity of $1129.8 \text{ mA h g}^{-1}$ and a charge capacity of $736.5 \text{ mA h g}^{-1}$, respectively. The corresponding initial coulombic efficiency is increased to 65.2% (Fig. 5b). It is reasonable to presume that the reoxidation from the $\text{Mn}/\text{Li}_2\text{O}$ nanocomposite to MnO nanoparticles occurs above the emf because of polarization. It is found that the capacity loss resulted from the above incomplete reoxidation is much larger for the MnO electrode by comparing the 1st charge profiles of both electrodes. Such large capacity loss is commonly attributed to the loss of electronic contact between the active particles or the polarization of electron transport. However, the latter has a slight effect on the charge capacity at the present rate of as low as $\text{C}/20$ (37.75 mA g^{-1}) considering the fact that the initial coulombic efficiency of MnO electrode is changeless (50.7%) when the current density is increased to 100 mA g^{-1} . Therefore, the large capacity loss in the charging process can be mainly attributed that only part of $\text{Mn}/\text{Li}_2\text{O}$ nanocomposites can be reoxidized owing to the loss of electronic contact between the active particles as a consequence of large volumetric changes during the conversion and de-conversion process. Obviously, the flexible RGOS anchored with MnO nanoparticle hybrid structure exhibits unique advantage to accommodate such intrinsic volumetric changes, leading to better electronic

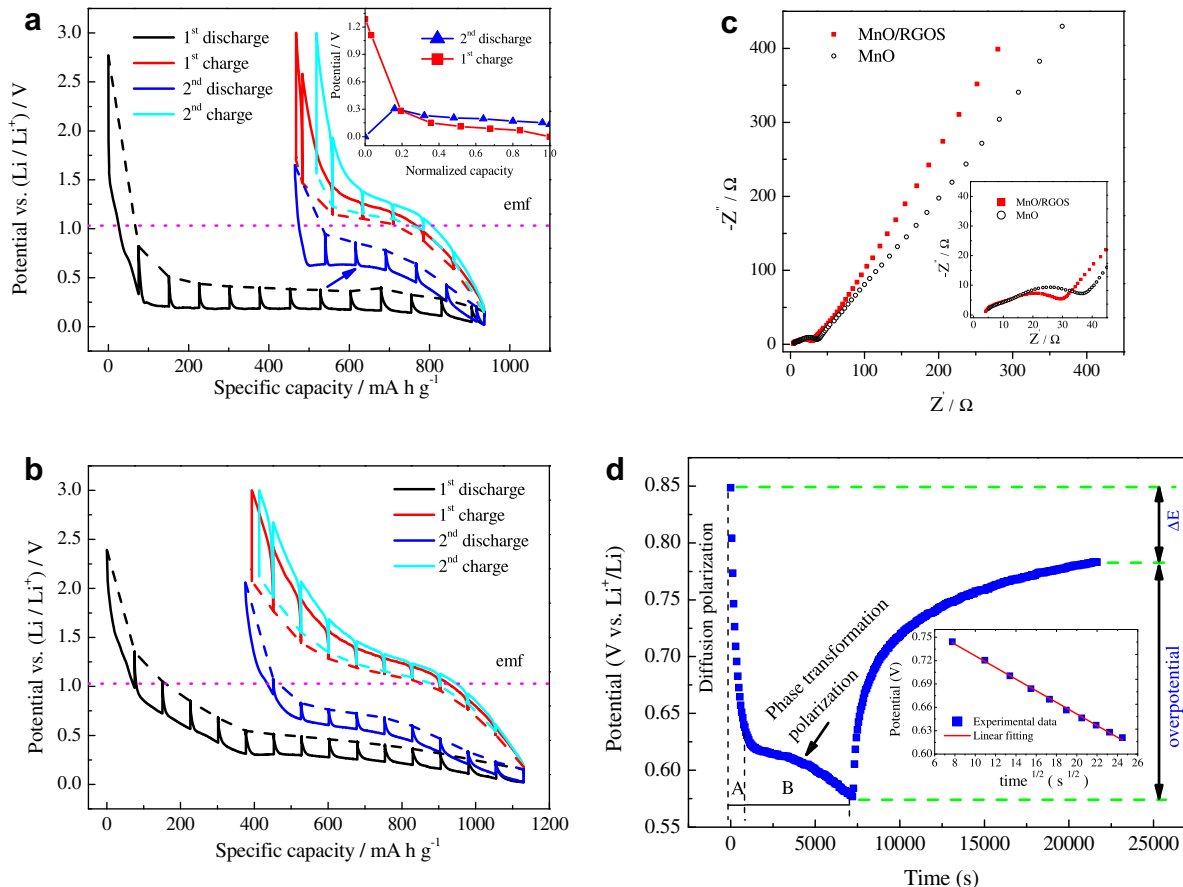


Fig. 5. GITT curves of (a) MnO and (b) MnO/RGOS electrodes. Solid lines are the GITT results. Dash lines are open-circuit potential and dot dash lines are the emf value. The inset is the difference estimated from the GITT curve between the cutoff potential and the open-circuit potential measured after relaxation. (c) Nyquist plots in the potential of 2.0 V (vs. Li/Li⁺) after rate cycling of the two measured electrodes (d) Discharge and following rest potential during GITT at the 3rd current pulses indicated by a blue arrow in Fig. 4a, and the inset is the plot of transient potential vs. square root of titration time and the linear fitting.

contact between the active particles. And this presumption is consistent with the HRTEM observation (Fig. 2c–e) of the cycled electrodes.

As the current rate increases, another contribution to the improved electrochemical performance of the MnO/RGOS electrode with respect to the MnO electrode is likely to have an origin in smaller penalty associated with electronic transport in electrode materials, especially, in the process of lithium extraction. This can be understood by the difference estimated from the GITT curves between the cutoff potential and the open-circuit potential measured after relaxation for the MnO electrode. As shown in the inset of Fig. 5a, 0 refers to full delithiation state and 1 refers to full lithiation state. Such differences can roughly reflect the polarization. It can be seen that this polarization slightly decreases with lithium insertion but continuously increases with the lithium extraction. In the term of electronic conductivity, this trend can be explained by the fact that, in the case of lithium insertion, the matrix Li₂O/Mn with a high electronic conductivity is expected due to insulating MnO being transformed into Mn nanoparticles. In contrast, in the case of lithium extraction, the electronic transport becomes increasingly problematic because of the expense of Mn nanoparticles to the formation of MnO nanoparticles. Given that the RGOS are good electronic conductors and the MnO nanoparticles are anchored on the surface of RGOS, it is expected that such nanostructure enables rapid electronic transport, which is good for lithium extraction, especially, when the electrode is operated at high rate. Indeed, the MnO/RGOS exhibits an enhanced rate capability with respect to the MnO electrode (Fig. 4d). And also

its reduced charge transfer impedance is supported by the EIS measurements carried out after the rate cycling for both electrodes. As shown in Fig. 5c, two depressed semicircles are observed for both the electrodes, including the one located at high frequency ranges corresponding to surface film resistance, and the one located at medium frequency ranges corresponding to charge transfer resistance. The inclined line at an approximate 45° angle to the real axis corresponds to the lithium-diffusion process within electrodes [44–47]. Obviously, the diameter of the second semicircle for the MnO/RGOS electrode is smaller than that of MnO. This indicates that the MnO/RGOS electrode displays smaller charge transfer impedance, facilitating the electronic transportation during the electrochemical reaction.

Another important issue is the reason for the staggering hysteresis in voltage observed between discharge and charge, which severely diminishes the round-trip efficiency of the electrode. GITT measurement has been widely used to study the thermodynamic and kinetic properties of the electrode materials [7,48,49]. Fig. 5d shows the GITT potential–time profiles at the 3rd discharge pulse. ΔE indicates the change in pseudo-equilibrium open-circuit potential before and after current pulses. Two distinct regions (A and B) of potential polarization are observed. The potential rapidly drops with time in region A and almost linearly decreases in region B. It is found that the potential exhibits a linear relationship with the square root of titration time in region A, as shown in the inset of Fig. 5d, indicative of a diffusion control region. However, it still cannot confirm whose diffusion, Li⁺ or O²⁻, dominates the polarization in this region. Especially, given that the

charge/discharge polarization obeys the order of metal hydrides < phosphides < nitrides < sulphides < oxides < fluorides [50], the polarization of conversion-type electrodes probably roots in poor mass transport kinetics of the anionic species which is governed by their electro-negativity and polarizability [36,50]. Further work is still going on to clarify this problem. The polarization in region B is well explained by the term of strain accommodation energy of phase transformation in the LiFePO₄ electrode [49]. Thus, the marked hysteresis in voltage has both thermodynamic and kinetic origins. And it is noteworthy that the hysteresis resulted from mass transport is obviously larger than that of energy penalty associated with phase transformation strain.

4. Conclusions

A simple strategy has been developed to synthesize MnO/RGOS hybrid. The obtained MnO particles are up to several nanometers in size and are homogeneously anchored on flexible and electrically conductive RGOS. As an anode material for LIBs, the unique microstructure of the hybrid can facilitate the electronic transportation and better accommodate the intrinsic volumetric changes, maintaining the structure integrity and leading to better electronic contact between the active particles during the lithium uptake/extraction. As a result, the hybrid material electrode shows superior lithium storage performance with respect to the MnO electrode. The corporation of RGOS is not very effective to decrease the hysteresis in voltage of MnO electrode, and such remark hysteresis has both thermodynamic and kinetic origins.

Acknowledgements

This work was supported by the Fundamental Research Funds for the Central Universities (2011QNA4006) and Key Science and Technology Innovation Team of Zhejiang Province (2010R50013).

References

- [1] P. Poizot, S. Laruelle, S. Grangeon, L. Dupont, J.M. Tarascon, *Nature* 407 (2000) 496–499.
- [2] A. Debart, L. Dupont, P. Poizot, J.B. Leriche, J.M. Tarascon, *J. Electrochem. Soc.* 148 (2001) A1266–A1274.
- [3] Y.J. Mai, S.J. Shi, D. Zhang, Y. Lu, C.D. Gu, J.P. Tu, *J. Power Sources* 204 (2012) 155–161.
- [4] H. Li, Z.X. Wang, L.Q. Chen, X.J. Huang, *Adv. Mater.* 21 (2009) 4593–4607.
- [5] H. Li, P. Balaya, J. Maier, *J. Electrochem. Soc.* 151 (2004) A1878–A1885.
- [6] X.Q. Yu, Y. He, J.P. Sun, K. Tang, H. Li, L.Q. Chen, X.J. Huang, *Electrochem. Commun.* 11 (2009) 791–794.
- [7] K.F. Zhong, X. Xia, B. Zhang, H. Li, Z.X. Wang, L.Q. Chen, *J. Power Sources* 195 (2010) 3300–3308.
- [8] T. Zhang, J. Gao, L.J. Fu, L.C. Yang, Y.P. Wu, H.Q. Wu, *J. Mater. Chem.* 17 (2007) 1321–1325.
- [9] X.H. Huang, J.P. Tu, C.Q. Zhang, J.Y. Xiang, *Electrochem. Commun.* 9 (2007) 1180–1184.
- [10] J.Y. Xiang, J.P. Tu, Y.F. Yuan, X.L. Wang, X.H. Huang, Z.Y. Zeng, *Electrochim. Acta* (2009) 1160–1165.
- [11] X.H. Xia, J.P. Tu, J.Y. Xiang, X.H. Huang, X.L. Wang, X.B. Zhao, *J. Power Sources* 195 (2010) 2014–2022.
- [12] L. Zhao, Y.-S. Hu, H. Li, Z. Wang, L. Chen, *Adv. Mater.* 23 (2011) 1385–1388.
- [13] B. Sun, Z.X. Chen, H.S. Kim, H. Ahn, G.X. Wang, *J. Power Sources* 196 (2011) 3346–3349.
- [14] Y.L. Ding, C.Y. Wu, H.M. Yu, J. Xie, G.S. Cao, T.J. Zhu, X.B. Zhao, Y.W. Zeng, *Electrochim. Acta* 56 (2011) 5844–5848.
- [15] J. Liu, Q.M. Pan, *Electrochim. Solid State Lett.* 13 (2010) A139–A142.
- [16] Y.M. Liu, X.Y. Zhao, F. Li, D.G. Xia, *Electrochim. Acta* 56 (2011) 6448–6452.
- [17] H. Xiang, K. Zhang, G. Ji, J.Y. Lee, C. Zou, X. Chen, J. Wu, *Carbon* 49 (2011) 1787–1796.
- [18] G. Wang, B. Wang, X. Wang, J. Park, S. Dou, H. Ahn, K. Kim, *J. Mater. Chem.* 19 (2009) 8378–8384.
- [19] X. Wang, X. Zhou, K. Yao, J. Zhang, Z. Liu, *Carbon* 49 (2011) 133–139.
- [20] J. Zhu, T. Zhu, X. Zhou, Y. Zhang, X.W. Lou, X. Chen, H. Zhang, H.H. Hng, Q. Yan, *Nanoscale* 3 (2011) 1084–1089.
- [21] Y. Zou, Y. Wang, *Nanoscale* 3 (2011) 2615–2620.
- [22] Z.-S. Wu, W. Ren, L. Wen, L. Gao, J. Zhao, Z. Chen, G. Zhou, F. Li, H.-M. Cheng, *ACS Nano* 4 (2010) 3187–3194.
- [23] Y.J. Mai, X.L. Wang, J.Y. Xiang, Y.Q. Qiao, D. Zhang, C.D. Gu, J.P. Tu, *Electrochim. Acta* 56 (2011) 2306–2311.
- [24] D.C. Marcano, D.V. Kosynkin, J.M. Berlin, A. Sinitskii, Z. Sun, A. Slesarev, L.B. Alemany, W. Lu, J.M. Tour, *ACS Nano* 4 (2010) 4806–4814.
- [25] G.M. Zhou, D.W. Wang, F. Li, L.L. Zhang, N. Li, Z.S. Wu, L. Wen, G.Q. Lu, H.M. Cheng, *Chem. Mater.* 22 (2010) 5306–5313.
- [26] Y. Si, E.T. Samulski, *Chem. Mater.* 20 (2008) 6792–6797.
- [27] I. Rusakova, T. Ould-Ely, C. Hofmann, D. Prieto-Centurión, C.S. Levin, N.J. Halas, A. Lütge, K.H. Whitmire, *Chem. Mater.* 19 (2007) 1369–1375.
- [28] S. Stankovich, D.A. Dikin, R.D. Piner, K.A. Kohlhaas, A. Kleinhammes, Y. Jia, Y. Wu, S.T. Nguyen, R.S. Ruoff, *Carbon* 45 (2007) 1558–1565.
- [29] D.V. Kosynkin, A.L. Higginbotham, A. Sinitskii, J.R. Lomeda, A. Dimiev, B.K. Price, J.M. Tour, *Nature* 458 (2009) 872–876.
- [30] A.L. Higginbotham, D.V. Kosynkin, A. Sinitskii, Z. Sun, J.M. Tour, *ACS Nano* 4 (2010) 2059–2069.
- [31] K.S. Subrahmanyam, S.R.C. Vivekchand, A. Govindaraj, C.N.R. Rao, *J. Mater. Chem.* 18 (2008) 1517–1523.
- [32] A. Gupta, G. Chen, P. Joshi, S. Tadigadapa, P.C. Eklund, *Nano Lett.* 6 (2006) 2667–2673.
- [33] V.C. Tung, M.J. Allen, Y. Yang, R.B. Kaner, *Nat. Nanotechnol.* 4 (2009) 25–29.
- [34] K. Zhong, B. Zhang, S. Luo, W. Wen, H. Li, X. Huang, L. Chen, *J. Power Sources* 196 (2011) 6802–6808.
- [35] J. Cabana, L. Monconduit, D. Larcher, M.R. Palacin, *Adv. Mater.* 22 (2010) E170–E192.
- [36] P.L. Taberna, S. Mitra, P. Poizot, P. Simon, J.M. Tarascon, *Nat. Mater.* 5 (2006) 567–573.
- [37] Y.J. Mai, J.P. Tu, C.D. Gu, X.L. Wang, *J. Power Sources* 209 (2012) 1–6.
- [38] H. Xia, M.O. Lai, L. Lu, *J. Mater. Chem.* 20 (2010) 6896–6902.
- [39] Y. Yu, C.-H. Chen, J.-L. Shui, S. Xie, *Angew. Chem., Int. Ed.* 44 (2005) 7085–7089.
- [40] P. Balaya, H. Li, L. Kienle, J. Maier, *Adv. Funct. Mater.* 13 (2003) 621–625.
- [41] J. Jamnik, J. Maier, *Phys. Chem. Chem. Phys.* 5 (2003) 5215–5220.
- [42] J. Maier, *Nat. Mater.* 4 (2005) 805–815.
- [43] H. Li, G. Richter, J. Maier, *Adv. Mater.* 15 (2003) 736–739.
- [44] Y.J. Mai, X.H. Xia, R. Chen, C.D. Gu, X.L. Wang, J.P. Tu, *Electrochim. Acta* 67 (2012) 73–78.
- [45] Y.J. Mai, J.P. Tu, X.H. Xia, C.D. Gu, X.L. Wang, *J. Power Sources* 196 (2011) 6388–6393.
- [46] J.C. Guo, X.L. Chen, C.S. Wang, *J. Mater. Chem.* 20 (2010) 5035–5040.
- [47] J.-G. Kang, Y.-D. Ko, J.-G. Park, D.-W. Kim, *Nanoscale Res. Lett.* 3 (2008) 390–394.
- [48] W.L. Liu, J.P. Tu, Y.Q. Qiao, J.P. Zhou, S.J. Shi, X.L. Wang, C.D. Gu, *J. Power Sources* 196 (2011) 7728–7735.
- [49] Y.J. Zhu, C.S. Wang, *J. Power Sources* 196 (2011) 1442–1448.
- [50] Y. Oumellal, A. Rougier, G.A. Nazri, J.M. Tarascon, L. Aymard, *Nat. Mater.* 7 (2008) 916–921.